

ADVANCES IN SIMULATION OF HIGH BRIGHTNESS/HIGH INTENSITY BEAMS

Ji Qiang*, LBNL, Berkeley, CA, USA

Abstract

High brightness/high intensity beams play an important role in accelerator based applications by driving x-ray free electron laser (FEL) radiation, producing spallation neutrons and neutrinos, and generating new particles in high energy colliders. In this paper, we report on recent advances in modeling the high brightness electron beam with application to the next generation FEL light sources and in modeling space-charge effects in high intensity proton accelerators.

START-TO-END SIMULATION OF MICROBUNCHING INSTABILITY EXPERIMENT IN AN FEL LINAC

The x-ray FEL provides a great tool for scientific discoveries in chemistry, physics, biology and material science. The microbunching instability seeded by shot noise and driven by collective effects (primarily space charge), can significantly degrade the quality of the electron beam before it enters the FEL undulators. Without proper control of the instability, the large final electron beam energy spread and phase space filamentation degrade the x-ray FEL performance [1–7]. The microbunching instability experiments recently carried out at the LCLS [8] provides a good opportunity to validate the computational model used in the simulation [9]. In the microbunching measurement at LCLS, the X-band transverse deflecting cavity (XTCAV) diagnostic [10] is located downstream of the undulator before the dump to measure the longitudinal phase space of the electron beam through the entire accelerator. The start-to-end beam dynamics simulations using the real number of electrons were done using a 3D parallel beam dynamics simulation framework IMPACT [11, 12]. It includes a time-dependent 3D space-charge code module IMPACT-T for injector modeling and a position-dependent 3D space-charge code module for linac and beam transport system model. The simulation starts from the generation of photo-electrons at the photocathode following the initial laser pulse distribution and the given initial thermal emittance. The electron macroparticles out of the cathode will be subject to both the external fields from a DC/RF gun and solenoid, and the space-charge/image charge fields from the Coulomb interaction of the particles among themselves. After exiting from the injector, the electron macroparticle will transport through a linear accelerator and beam transport system that includes laser heater, bunch compressors, accelerating RF cavities, harmonic linearizer, and magnetic focusing elements. Besides the 3D space-charge effects, the simulation also includes coherent synchrotron radiation (CSR) effects through a bending magnet,

incoherent synchrotron radiation inside the bending magnet, RF cavity structure wakefield, and resistive wall wakefield. In the simulations, we track the beam down to the XTCAV screen and compare with the measurements. Figure 1 shows the final longitudinal phase space after the XTCAV from the experimental observation and from the simulation with laser heater turned off for the 1 kA study case.

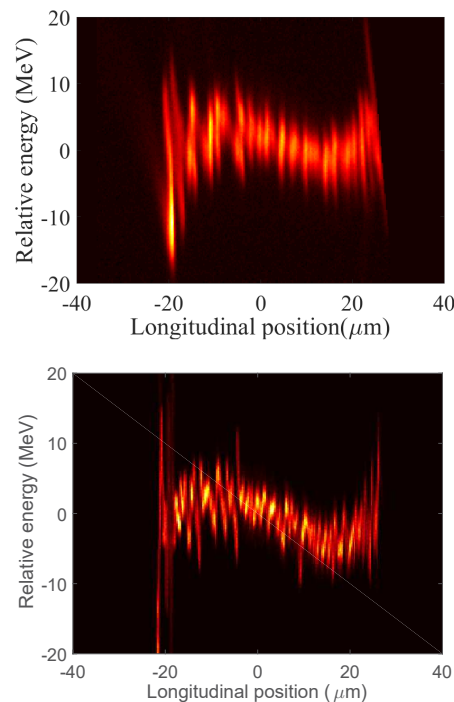


Figure 1: Measurement (top) and simulation (bottom) of the final longitudinal phase space distribution with the laser heater off. Beam current is 1 kA, with bunch charge 180 pC. The bunch head is to the right.

Here, a strong phase space fluctuation due to the microbunching instability can be seen from both the measurement and the simulation. There is no external seeded initial modulation. This large fluctuation arises from the shot-noise inside the beam and is amplified by collective effects, especially space charge effects through the accelerator.

The microbunching instability can be suppressed through Landau damping by increasing the electron beam uncorrelated energy spread before the bunch compressor using the laser heater. Figure 2 shows the final longitudinal phase space after the XTCAV from both the measurement and the simulation with extra 19 keV uncorrelated slice energy spread from the laser heater. The phase space fluctuation is significantly reduced with the use of the laser heater. This is observed in both the measurement and the simulation.

* jqiang@lbl.gov

Content from this work may be used under the terms of the CC BY 3.0 licence (© 2018). Any distribution of this work must maintain attribution to the author(s), title of the work, publisher, and DOI.

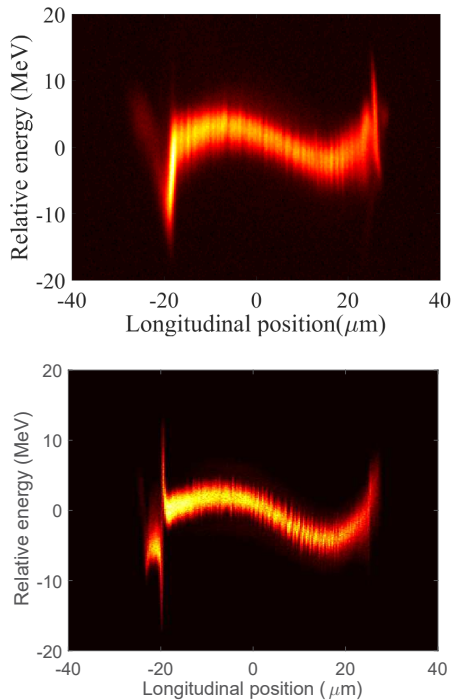


Figure 2: Measurement (top) and simulation (bottom) of the final longitudinal phase space distribution with the laser heater at 19 keV.

The simulation also shows a similar time-energy correlation in the longitudinal phase space to the measurement. The energy dip around the head of the distribution (at $\sim 15 \mu\text{m}$ in Fig. 2) comes from the effects of resistive wall wakefield in the long, narrow undulator chamber. The dip near the tail of the distribution is due to the longitudinal space-charge and coherent synchrotron radiation effects from the large current spike near the tail of the electron beam.

GLOBAL OPTIMIZATION OF A NEXT GENERATION LIGHT SOURCE DESIGN

In previous studies, the design optimizations of the injector and the linac were done separately. In recent study, we combined the control parameters in the injector and the linac together into a single group of control parameters through start-to-end simulation for global beam dynamics design optimization [13]. Figure 3 shows a schematic plot of the global optimization including both the injector control parameters and the linac control parameters in the start-to-end beam dynamics optimization. Here, the start-to-end simulation is treated as an objective function in the parallel multi-objective optimizer. The parallel optimizer will call the IMPACT simulation by passing the injector control parameters and the linac control parameters into the objective function. The injector control parameters normally include laser pulse transverse size and length, RF gun amplitude and phase, solenoid strength, buncher and boosting cavity amplitudes and phases. The linac control parameters include linac section 1 cavity amplitude and phase, harmonic linearizer amplitude and phase, bunch compressor 1 bending

angle, linac section 2 cavity amplitude and phase, bunch compressor 2 bending angle, and so on.

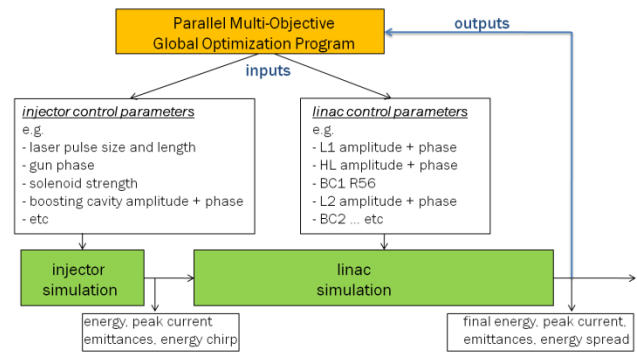


Figure 3: A schematic diagram of the global beam dynamics optimization.

Instead of starting with direct global optimization in the entire control parameter space, we start the optimization with reduced control parameter space that contains only the injector control parameters. The two objective functions, final project transverse emittance and rms bunch length (directly related to peak current) at the exit of the injector are optimized subject to a number of constraints. These constraints are final electron beam energy, beam energy chirp, longitudinal phase space nonlinearity, and so on. After a Pareto optimal front is found for these two objective functions at the exit of the injector, these optimal injector control parameters are combined with some randomly sampled control parameter solutions in the linac. Using the optimal injector control parameters as a partial initial component in the global control parameter solution significantly saves the computational time and speeds up the convergence of the final global solution. During the global beam dynamics optimization, one of the objective (transverse emittance) from the original injector optimization becomes a constraint to the new objective functions. Those solutions at the exit of the injector that can not satisfy this constraint for final start-to-end optimization will be automatically excluded at the beginning of the global optimization. Two objective functions are defined for the global longitudinal beam dynamics optimization. These two functions are fraction of charge and rms energy spread inside a given longitudinal window. The output from the injector such as energy, emittance, and energy spread are used as constraints for the global optimization. Besides the constraint at the exit of the injector, we also put constraints at the final linac output such as energy, peak current etc.

As an application, we applied the above global multi-objective beam dynamics optimization tool to an LCLS-II design optimization with a 20 pC charge. The LCLS-II is a high repetition rate (1 MHz) x-ray FEL that will deliver photons of energy between 200 eV and 5 keV [14, 15]. For the global longitudinal beam dynamics optimization of this accelerator, we have defined 22 control parameters: 12 in the injector, 10 in the linac. Figure 4 shows the Pareto front of the two objective functions from the global opti-

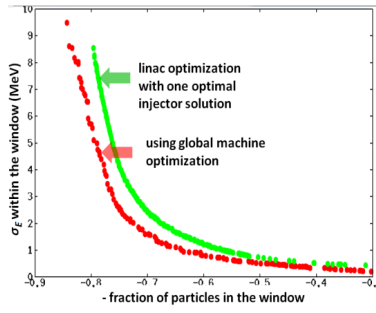


Figure 4: The Pareto front from the global beam dynamics optimization and from the linac only optimization using one optimal injector solution.

mization. These two objective functions are the negative fraction of charge inside and the rms energy spread inside a window between -7 and $9 \mu\text{m}$. In this plot, we also show the Pareto front from only the linac optimization using a solution from the injector as an initial distribution. It is seen that the Pareto front from the global optimization is significantly better than that from the linac only optimization. For the same amount of charge inside the window, the global solution has 40% less energy spread in some region. For the same level of the final rms energy spread, the global solution has 15% larger amount of charge. In this simulation besides those constraints for the beam at the exit of the injector, we also put constraints on the final beam energy to be greater than 3.9 GeV , final rms energy spread to be less than 2.5 MeV , fraction of charge inside the window between 0.3 and 0.9 . Figure 5 shows the final electron beam current profile from a solution without and with global design optimization. It is seen that the final current profile is significantly improved through the global optimization. This results in more than 50% improvement in the final FEL radiation pulse energy [16].

A FULLY SYMPLECTIC MODEL FOR SELF-CONSISTENT SPACE-CHARGE SIMULATION

The numerical symplectic integrator is important in long-term tracking simulation in order to preserve phase space structure. In the self-consistent symplectic particle-in-cell (PIC) model [17, 18], macroparticle phase space coordinate advancing through a single step τ can be given as:

$$\begin{aligned} \zeta(\tau) &= \mathcal{M}(\tau)\zeta(0) \\ &= \mathcal{M}_1(\tau/2)\mathcal{M}_2(\tau)\mathcal{M}_1(\tau/2)\zeta(0) + O(\tau^3) \end{aligned} \quad (1)$$

where the transfer map \mathcal{M}_1 corresponds to the single particle Hamiltonian including external fields and the transfer map \mathcal{M}_2 corresponds to the space-charge potential from the multi-particle Coulomb interactions. The numerical integrator Eq. 1 will be symplectic if both the transfer map \mathcal{M}_1 and the transfer map \mathcal{M}_2 are symplectic. For a coasting beam inside a rectangular perfectly conducting pipe, the space-charge potential can be obtained from the solution of the

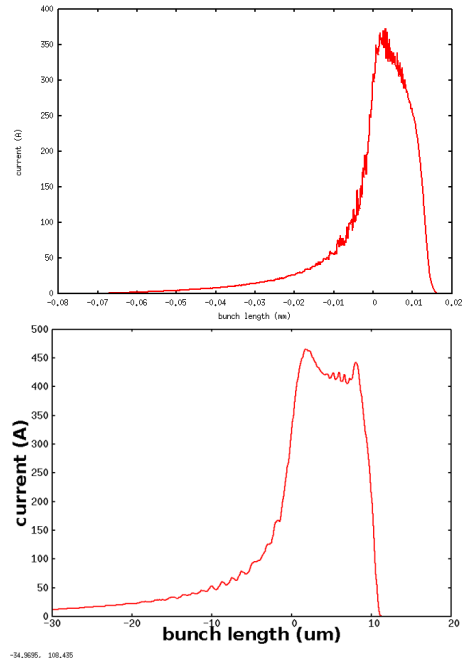


Figure 5: The final electron beam current profile before (top) and after (bottom) global optimization.

Poisson equation using a spectral method. The one-step symplectic transfer map \mathcal{M}_2 of particle i from the space-charge Hamiltonian is given as:

$$x_i(\tau) = x_i(0) \quad (2)$$

$$y_i(\tau) = y_i(0) \quad (3)$$

$$p_{xi}(\tau) = p_{xi}(0) - \tau 4\pi K \sum_I \sum_J \frac{\partial S(x_I - x_i)}{\partial x_i} \times S(y_J - y_i) \phi(x_I, y_J) \quad (4)$$

$$p_{yi}(\tau) = p_{yi}(0) - \tau 4\pi K \sum_I \sum_J S(x_I - x_i) \times \frac{\partial S(y_J - y_i)}{\partial y_i} \phi(x_I, y_J) \quad (5)$$

where both p_{xi} and p_{yi} are normalized by the reference particle momentum p_0 , $K = qI/(2\pi\epsilon_0 p_0 v_0^2 \gamma_0^2)$ is the generalized perveance, I is the beam current, ϵ_0 is the permittivity of vacuum, p_0 is the momentum of the reference particle, v_0 is the speed of the reference particle, γ_0 is the relativistic factor of the reference particle, $S(x)$ is the unitless shape function (also called deposition function in the PIC model), and the ϕ is given as:

$$\begin{aligned} \phi(x_I, y_J) &= \frac{4}{ab} \sum_{l=1}^{N_l} \sum_{m=1}^{N_m} \frac{1}{\gamma_{lm}^2} \sum_{I'} \sum_{J'} \bar{\rho}(x_{I'}, y_{J'}) \times \\ &\quad \sin(\alpha_l x_{I'}) \sin(\beta_m y_{J'}) \sin(\alpha_l x_I) \sin(\beta_m y_J) \end{aligned} \quad (6)$$

where a and b are the horizontal (x) and the vertical (y) aperture sizes respectively, $\alpha_l = l\pi/a$, $\beta_m = m\pi/b$, $\gamma_{lm}^2 = \alpha_l^2 + \beta_m^2$, the integers I, J, I' , and J' denote the two dimensional computational grid index, and the summations with

respect to those indices are limited to the range of a few local grid points depending on the specific deposition function. The density related function $\bar{\rho}(x_{I'}, y_{J'})$ on the grid can be obtained from:

$$\bar{\rho}(x_{I'}, y_{J'}) = \frac{1}{N_p} \sum_{j=1}^{N_p} S(x_{I'} - x_j) S(y_{J'} - y_j), \quad (7)$$

In the PIC literature, compact shape functions are used in the simulation. For example, a quadratic shape function can be written as [19, 20]:

$$S(x_I - x_i) = \begin{cases} \frac{3}{4} - \frac{(x_i - x_I)^2}{\Delta x}, & |x_i - x_I| \leq \Delta x/2 \\ \frac{1}{2} \left(\frac{3}{2} - \frac{|x_i - x_I|}{\Delta x} \right)^2, & \Delta x/2 < |x_i - x_I| \leq 3/2 \Delta x \\ 0 & \text{otherwise} \end{cases} \quad (8)$$

$$\frac{\partial S(x_I - x_i)}{\partial x_i} = \begin{cases} -2 \frac{(x_i - x_I)}{\Delta x} / \Delta x, & |x_i - x_I| \leq \Delta x/2 \\ \left(-\frac{3}{2} + \frac{(x_i - x_I)}{\Delta x} \right) / \Delta x, & \Delta x/2 < |x_i - x_I| \leq 3/2 \Delta x, x_i > x_I \\ \left(\frac{3}{2} + \frac{(x_i - x_I)}{\Delta x} \right) / \Delta x, & \Delta x/2 < |x_i - x_I| \leq 3/2 \Delta x, x_i \leq x_I \\ 0 & \text{otherwise} \end{cases} \quad (9)$$

where Δx is the mesh size in x dimension. The same shape function and its derivative can be applied to the y dimension.

Figure 6 shows the 4D emittance growth $(\frac{\epsilon_x}{\epsilon_{x0}} \frac{\epsilon_y}{\epsilon_{y0}} - 1)\%$ evolution from the symplectic PIC model and those from the nonsymplectic PIC model with the same nominal step size, from the nonsymplectic PIC model with one-half of the nominal step size, and from the nonsymplectic PIC model with one-quarter of the nominal step size. It is seen that as the step size decreases, the emittance growth from the nonsymplectic PIC model converges towards that from the symplectic PIC model.

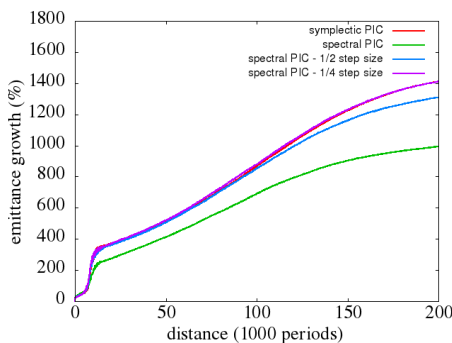


Figure 6: Four dimensional emittance growth evolution from the symplectic PIC model, and the nonsymplectic spectral PIC.

ANALYSIS AND MITIGATION OF ARTIFICIAL EMITTANCE GROWTH

In the long-term macroparticle space-charge tracking simulation, even with the use of self-consistent symplectic space-charge model, there still exists numerical emittance growth.

SAPLG01

The cause of this numerical artificial emittance growth can be understood using a one-dimensional model. Following the spectral method used in the above symplectic PIC model for the space-charge potential, we calculated the sine function expansion mode amplitude from a smooth density distribution function on the grid and from a macroparticle sampled distribution function depositing onto the grid. Here, the amplitude of density mode l from the sampled macroparticle deposition is given as:

$$\rho^l = \frac{1}{N_p} \frac{2}{N_g \Delta x} \sum_i \sum_I S(x_I - x_i) \sin(\alpha_l x_i) \quad (10)$$

where N_p is the total number of macroparticles and N_g is the total number of grid cells. Figure 7 shows the mode amplitude as a function of mode number from the smooth Gaussian function on the grid, from the linear particle deposition, from the quadratic particle deposition, and from the Gaussian kernel particle deposition on the grid using 25,000 macroparticles and 128 grid cells. Here, the Gaussian kernel

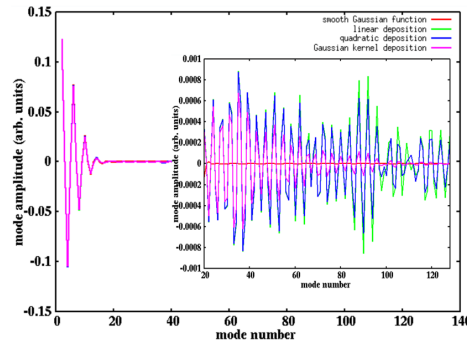


Figure 7: The spectral mode amplitude of a Gaussian distribution as a function of mode number from the smooth Gaussian function on the grid (red), from the linear particle deposition (green), the quadratic particle deposition (blue), and the Gaussian kernel particle deposition on the grid (magenta).

particle deposition shape function is defined as:

$$S(x_I - x_i) = \begin{cases} \exp\left(-\frac{(x_i - x_I)^2}{2\sigma^2}\right); & |x_i - x_I| \leq 3.5\sigma \\ 0; & \text{otherwise} \end{cases} \quad (11)$$

and σ is the chosen as the mesh size. It is seen that for the smooth Gaussian distribution function, with mode number beyond 20, the mode amplitude is nearly zero while the mode amplitude from the macroparticle deposition fluctuates with a magnitude of about 10^{-4} . Those nonzero high frequency modes cause fluctuation in density distribution and induce extra numerical emittance growth. The higher order deposition scheme spreads the macroparticle across multiple grid points and reduces the density fluctuation. However, the Gaussian kernel deposition is computationally much more expensive in comparison to the other two deposition methods.

The above fluctuation of the density mode amplitude from macroparticle deposition can be estimated quantitatively us-

ing the standard deviation (or variance) of the mode amplitude. Given the mode amplitude ρ^l in Eq. 10, the variance of ρ^l is given as:

$$\text{var}(\rho^l) = \frac{1}{N_p} \text{var}\left(\frac{2}{N_g \Delta x} \sum_I S(x_I - x_i) \sin(\alpha_l x_i)\right) \quad (12)$$

where

$$\text{var}\left(\frac{2}{N_g \Delta x} \sum_I S(x_I - x_i) \sin(\alpha_l x_i)\right) = \frac{1}{N_p} \left(\frac{2}{N_g \Delta x}\right)^2 \sum_i \left[\sum_I S(x_I - x_i) \sin(\alpha_l x_i) \right]^2 - (\rho^l)^2 \quad (13)$$

Figure 8 shows the mode amplitude standard deviation as a function of mode number for the above Gaussian function by using the linear deposition, the quadratic deposition, and the Gaussian kernel deposition. The mode amplitude standard deviation is small at small mode number and grows quickly to 10^{-4} level and start to decrease after about 10 modes. The standard deviation among the three deposition schemes

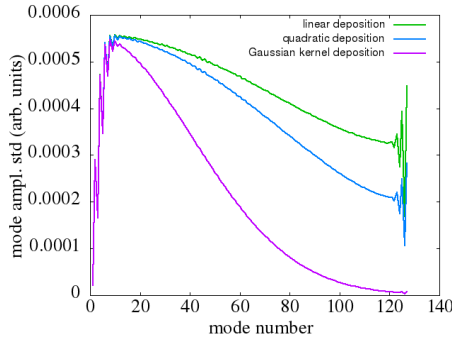


Figure 8: Mode amplitude standard deviation as a function of mode number from the linear particle deposition (green), the quadratic particle deposition (blue), and the Gaussian kernel particle deposition on the grid (magenta) using 25,000 macroparticles and 128 grid cells.

becomes smaller as the order of deposition scheme becomes higher.

The error in the charge density mode amplitude results in error in the solution of space-charge potential and the corresponding force in momentum update in Eqs. 4-5. Assume that the error of force in x momentum update is δF , after one step τ , the emittance growth due to this error will be:

$$\Delta\epsilon \approx (\langle x^2 \rangle \langle x' \delta F \rangle - \langle x x' \rangle \langle x \delta F \rangle) \tau / \epsilon + \frac{1}{2} (\langle x^2 \rangle \langle (\delta F)^2 \rangle - \langle x \delta F \rangle^2) \tau^2 / \epsilon \quad (14)$$

where $\langle \rangle$ denotes the average with respect to the particle distribution. If δF is a linear function of the position x , the emittance growth will be zero as expected since the linear force will not change the beam emittance. If δF is a random error force with zero mean and independent of x and x' , the emittance growth would be

$$\frac{\Delta\epsilon}{\tau} \approx \frac{1}{2} \langle x^2 \rangle \langle (\delta F)^2 \rangle / \epsilon \quad (15)$$

Assume that this error is due to mode amplitude fluctuation of the finite number of macroparticles sampling, from the above example, we see that $\langle (\delta F)^2 \rangle \propto 1/N_p$. This suggests that the numerical emittance growth would decrease as more macroparticles are used. If δF is not a purely random error force (e.g. due to systematic truncation error), the dependence of the emittance growth on the number of macroparticle is more complicated. Figure 9 shows the 4D emittance growth rate from the emittance growth evolution as a function of macroparticle number in a linear FODO lattice and a nonlinear FODO and sextupole lattice. Here, the

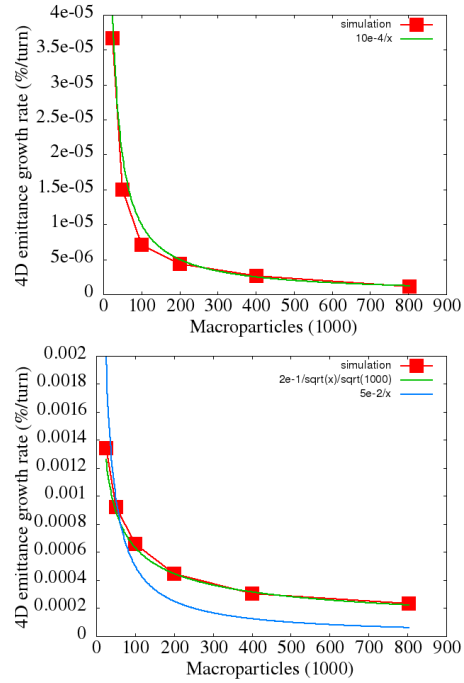


Figure 9: The 4D emittance growth rate as a function of the simulation macroparticle number using a linear FODO lattice (top) and a FODO and sextupole lattice (bottom).

lattice consists of 10 focusing-drift-defocusing-drift (FODO) lattice periods and one sextupole element per turn. The zero current tune of the lattice is 2.417. With 30 A beam current, the corresponding linear space-charge tune shift is 0.113. It is seen that in the linear lattice (no sextupole), the emittance growth rate scales as $1/N_p$ which is expected from the random sampling errors. In a nonlinear lattice, the emittance growth rate scales close to $1/\sqrt{N_p}$. This slower scaling with respect to the macroparticle number N_p might be due to the interaction between the numerical force error and the nonlinear resonance.

The charge density fluctuation from the macroparticle sampling can be further smoothed out by using a numerical filter in frequency domain besides employing the shape function for particle deposition. Instead of using a standard cut-off method that removes all modes beyond a given mode number (i.e. cut-off frequency), we proposed using an amplitude threshold method to remove unwanted modes. The mode with an amplitude below the threshold value is re-

Content from this work may be used under the terms of the CC BY 3.0 licence (© 2018). Any distribution of this work must maintain attribution to the author(s), title of the work, publisher, and DOI.

moved from the density distribution. The advantage of this method is instead of removing all high frequency modes, it will keep the high frequency modes with large amplitudes. These modes can represent real physics structures inside the beam. The threshold also removes the unphysical low frequency modes associated with the small number of macroparticle sampling. Here, we explored two threshold methods. In the first threshold method, the threshold value is calculated from a given fraction of the maximum amplitude of the density spectral distribution. In the second method, the threshold value is defined as a few standard deviations of the mode amplitude as shown in the one-dimensional Gaussian function example. The mode with an amplitude below the threshold value is regarded as numerical sampling error due to the use of small number of macroparticles and is removed from the density distribution. The advantage of the first method is that the threshold value is readily attainable from the density spectral distribution. The disadvantage of this method is that the threshold fraction is an external supplied hyperparameter. The advantage of the second method is that the threshold value is calculated dynamically through the simulation. The disadvantage of this method is the high computational cost to obtain the standard deviation of each mode. The total computational cost of those standard deviations is proportional to the number of modes multiplied by the number of macroparticles.

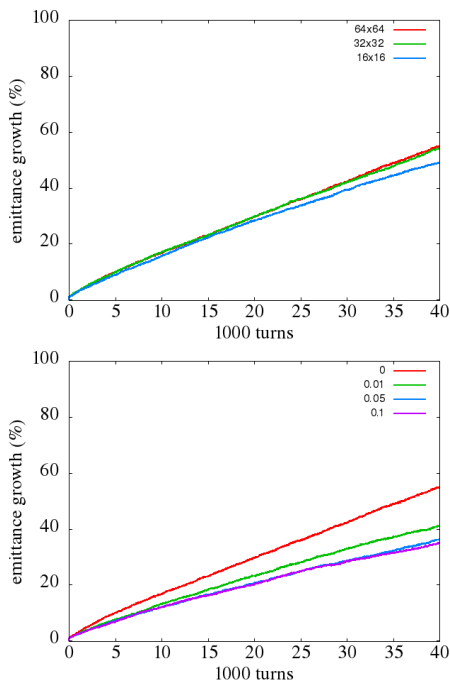


Figure 10: The 4D emittance growth using 64×64 , 32×32 , 16×16 modes (top) and with 0 (no filtering) with 0.01, 0.05 and 0.1 threshold filtering (bottom) of charge density distribution using 25k macroparticles in a FODO and sextupole lattice.

We ran the simulation of 30A proton beam transport in the lattice including nonlinear sextupole element. The 4D

emittance growth evolutions using the brute force cut-off and the threshold filtering are shown in Fig. 10. It is seen that even with 16×16 mode cut-off filtering, there still exists significant emittance growth, while a threshold value 0.1 helps significantly lower the emittance growth. Using the four-sigma standard deviation threshold value yields similar emittance growth to the fraction threshold (0.1) as shown in Fig. 11. Those emittance growths include both the physical resonance driven emittance growth and the numerical error driven artificial emittance growth.

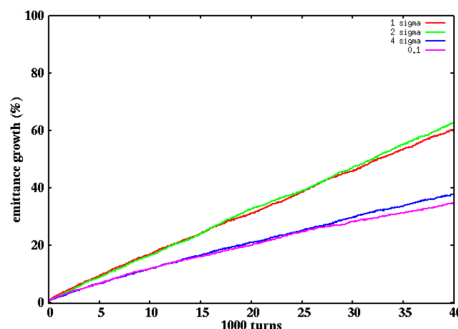


Figure 11: 4D emittance growth with one sigma, two sigma, four sigma standard deviation and 0.1 maximum amplitude threshold filtering of charge density distribution using 25k macroparticles in a FODO and sextupole lattice.

SUMMARY

In this paper, we have shown that the microbunching instability associated with the high brightness electron beam in a x-ray FEL linac experiment can be well reproduced through the start-to-end simulation using real number of electrons. The global design optimization including both the injector control parameters and the linac control parameters significantly improves the final electron beam longitudinal phase space distribution. The accuracy of simulating a high intensity proton beam can be improved through the use of a fully self-consistent symplectic space-charge model. The artificial numerical emittance growth in the long-term space-charge simulation can be mitigated by using a threshold based numerical filter in frequency domain.

ACKNOWLEDGMENT

This work was supported by the U.S. Department of Energy under Contract No. DE-AC02-05CH11231 and used computer resources at the National Energy Research Scientific Computing Center.

REFERENCES

- [1] M. Borland *et al.*, *Nucl. Instrum. Methods Phys. Res.*, Sect. A, vol. 483, pp. 268, 2002.
- [2] E. L. Saldin, E. A. Schneidmiller, and M. V. Yurkov, *Nucl. Instrum. Methods Phys. Res.*, Sect. A, vol. 483, pp. 516, 2002.
- [3] Z. Huang, M. Borland, P. Emma, J. Wu, C. Limborg, G. Stupakov, and J. Welch, *Phys. Rev. ST Accel. Beams*, vol. 7, pp. 074401, 2004.

- [4] M. Venturini, R. Warnock, and A. A. Zholents, *Phys. Rev. ST Accel. Beams*, vol. 10, pp. 054403, 2007.
- [5] J. Qiang, R. D. Ryne, M. Venturini, A. A. Zholents, and I. V. Pogorelov, *Phys. Rev. ST Accel. Beams*, vol. 12, pp. 100702, 2009.
- [6] S. Di Mitri, M. Cornacchia, S. Spampinati, and S. Milton, *Phys. Rev. ST Accel. Beams*, vol. 13, pp. 010702, 2010.
- [7] J. Qiang, C. E. Mitchell, M. Venturini, *Phys. Rev. Lett.*, vol. 111, pp. 054801, 2013.
- [8] D. Ratner, C. Behrens, Y. Ding, Z. Huang, A. Marinelli, T. Maxwell, and F. Zhou, *Phys. Rev. ST Accel. Beams*, vol. 18, pp. 030704, 2015.
- [9] J. Qiang, Y. Ding, P. Emma, Z. Huang, D. Ratner, T. O. Raubenheimer, and F. Zhou, *Phys. Rev. Accel. Beams*, vol. 20, pp. 054402, 2017.
- [10] C. Behrens *et al.*, *Nature Communications*, vol. 5, pp. 3762, 2014.
- [11] J. Qiang, R. Ryne, S. Habib, V. Decyk, *J. Comp. Phys.*, vol. 163, pp. 434, 2000.
- [12] J. Qiang, S. Lidia, R. D. Ryne, and C. Limborg-Deprey, *Phys. Rev. ST Accel. Beams*, vol. 9, pp. 044204, 2006.
- [13] J. Qiang, "Start-to-end beam dynamics optimization of x-ray FEL light source accelerators," in *Proc. NAPAC'16*, Chicago, IL, USA, Oct 2016. doi:10.18429/JACoW-NAPAC2016-WEA3I002
- [14] T. O. Raubenheimer, "Technical challenges of the LCLS-II CW X-ray FEL," in *Proc. IPAC'15*, Richmond, VA, USA, May 2015. doi:10.18429/JACoW-IPAC2015-WEYC1
- [15] P. Emma *et al.*, "Linear accelerator design for the LCLS-II FEL facility," in *Proc. FEL'14*, Basel, Switzerland, THP025, Aug. 2014.
- [16] G. Marcus and J. Qiang, "LCLS-II SCRF start-to-end simulations and global optimization as of September 2016," LCLS-II TN-1704, 2017.
- [17] J. Qiang, *Phys. Rev. Accel. Beams*, vol. 20, pp. 014203, 2017.
- [18] J. Qiang, *Phys. Rev. Accel. Beams*, vol. 21, pp. 054201, 2018.
- [19] R. W. Hockney and J. W. Eastwood, *Computer Simulation Using Particles*, Adam Hilger, New York, 1988.
- [20] C. K. Birdsall and A. B. Langdon, *Plasma Physics Via Computer Simulation*, Taylor and Francis, New York, 2005.